Electronic and magnetic properties of ZnS doped with Cr

C. Tablero*
Instituto de Energía Solar, Universidad Politécnica de Madrid, Ciudad Universitaria s/n, 28040 Madrid, Spain
(Received 7 June 2006; revised manuscript received 7 August 2006; published 8 November 2006)

Materials with an isolated partially filled intermediate band are of great interest as new materials for high-efficiency solar cells, as up- and down-converters, and midinfrared lasers with low nonradiative decay because of the properties of this band. This intermediate band is only present in some compounds, such as a ZnS host semiconductor uniformly doped with Cr. The study presented in this work is based on the substitutional doping of Cr by Zn with atomic concentrations of 3.125%. We use first principles with the local density approximation. To improve the description of the localized states a screened Coulomb interaction has been applied. From the results, it was found that these materials have a partially filled intermediate band for both ferromagnetic and antiferromagnetic spin alignments. The addition of a Hubbard term from 0 to 9 eV shows a greater stability of the ferromagnetic spin order and an increase in the intermediate bandwidth.

DOI: 10.1103/PhysRevB.74.195203 PACS number(s): 71.20.Nr, 71.55.−i, 71.28.+d

I. INTRODUCTION

Since the model of a new solar cell was proposed,[1] there has been increasing interest in research into solid-state materials with the appropriate characteristics. These new solar cells are characterized by a full band [valence band (VB)], an empty band [conduction band (CB)], and a partially filled intermediate band (IB). For the absorption of photons to be more efficient than in conventional cells the IB must be partially filled to permit the absorption of low-energy photons to pass the electrons from the VB to the partially filled IB and from there to the CB. Therefore, the Fermi energy must lie in the IB. This kind of solar cell may present efficiencies higher than those established by the Shockley limit,[2] as has been demonstrated in previous works.[1]

A schematic band diagram is shown in Fig. 1. The lower-energy photons ($h\nu_{VI}$ and $h\nu_{IC}$ in Fig. 1) can promote electrons from the VB to the IB and from the IB to the CB, creating additional electron-hole pairs with respect to those created by photons ($h\nu_{VC}$ in Fig. 1) which cause electrons from the VB to pass on to the CB. Therefore, the current is enhanced. In addition, the output voltage of the cell is maintained because it is limited by the gap between the CB and VB (ΔE_{VC}) and not by the band gaps between the VB and IB (ΔE_{VI}) and IB-CB (ΔE_{IC}).[1] This is a result of the separation between bands and the consequent description of the carrier population in each band by its own quasi-Fermi levels. In the operation mode (Fig. 1), the electron and hole quasi-Fermi levels split and the output voltage is proportional to the chemical potential between the VB and CB. As a result, the power and limiting efficiency are increased. This limiting efficiency has been found to be 63.2% in contrast to 40.7% of conventional single-gap solar cells.

This basic electronic band structure corresponding to a conceptually new class of materials, well known as intermediate band materials, is also characteristic of transparent conducting oxides. The introduction of an IB into the band gap of an insulating host material would help to keep intense interband transitions (from the VB to the IB and from the IB to the CB) above the visible range. Furthermore, the IB should be narrow enough to keep intraband transitions below the visible range. This requires appropriate values for both the gaps and IB bandwidth.

The solid-state materials studied with these characteristics are based on quantum dots and semiconductors with a high transition-metal impurity concentration. Quantum dots[3] have been proposed and manufactured. Possible intermediate-band materials have also been manufactured from II–VI-diluted oxides.[4] Extensive studies using first principles on materials based on III–V host semiconductors where the impurity is a transition metal have recently been carried out.[5] Diluted magnetic semiconductors based on III–V and II–VI semiconductors doped with different transition metals and concentration substituting to cation[6–8] have also been studied. An IB has been described for the substitutional doping of Ga by Mn in GaN host semiconductors with concentrations of 1.56% and 3.125% (Ref. 6) and Cr by Ga in GaP with concentrations of 3% (Ref. 7).

Several new tunable lasers with a high quantum yield based on transition-metal-doped zinc chalcogenides with concentrations of the order of 10^{19} cm^{-3} have also been stud-

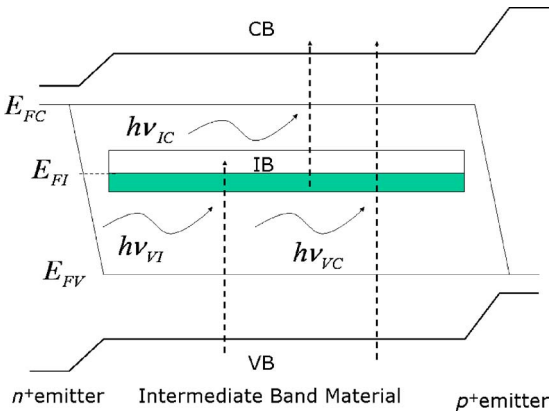

FIG. 1. (Color online) Schematic band diagram of an intermediate-band material showing the band gaps, photon generation process, and quasi-Fermi levels of the intermediate-band solar cell in a nonequilibrium situation. The electrons in the three bands are described by their own quasi-Fermi levels: E_{FV}, E_{FI}, and E_{FC} by the VB, IB, and CB.

ied using spectroscopic techniques.[9] From these results, highly favorable lasers for the midinfrared are produced when Cr is a dopant in the zinc chalcogenides because only the Cr appears to be significantly free from the negative effects of nonradiative decay.

One useful approach to obtaining and understanding the electronic and optical properties of these materials is the first-principles electronic approach. In this work we present an analysis of the electronic properties of a material derived from the ZnS host semiconductor where the Cr is incorporated, substituting the host metallic atom (two Cr for each of the 32 Zn atoms) using *ab initio* calculations. This material has the appropriate characteristics of the new high efficiency solar-cell prototype. Moreover, these materials with different transition-metal atom dilution have been produced experimentally as has previously been mentioned. Nevertheless, we are interested in the relationship between the macroscopic characteristic and the microscopic properties. In particular, the new high-efficiency solar cells and the new tunable lasers with a high quantum yield based on transition-metal-doped zinc chalcogenides have a common microscopic characteristic: the partially full intermediate band. We believe that this characteristic is responsible for the decrease of the nonradiative recombination for both lasers and solar cells.[10] Analyzing the physical causes of the nonradiative recombination, an increase in the impurity density to the point of forming an IB can lead to the suppression of nonradiative Shockley-Read-Hall (SRH) recombination. In this case, the distribution of the trapped electron charge density between all impurities prevents the appearance of strong localized charge variations and thus the displacement of the trapping impurities responsible for the nonradiative SRH recombination.

The paper is organized as follows: a description of the numerical methodology used for this study is presented in Sec. II. The results of several electronic properties are presented and analyzed in Sec. III. We conclude with a discussion on the summary of the results in Sec. IV.

II. CALCULATIONS

The electronic structure calculations were carried out by using the density functional theory (DFT) method based on pseudopotentials for core electrons and numerically localized pseudoatomic orbitals as the basis set for the valence wave functions. The standard Kohn-Sham[11] (KS) equations are solved self-consistently.[12] For the exchange and correlation term, the LDA has been used as proposed by Ceperley and Alder.[13] The standard Troullier-Martins[14] pseudopotential is adopted and expressed in the Kleinman-Bylander[15] factorization. The KS orbitals are represented using a linear combination of confined pseudoatomic orbitals.[16] An analysis of the basis set convergence has also been carried out using from single ζ to double ζ with polarization basis sets for all atoms and varying the number of the special k points in the irreducible Brillouin zone. In all calculations a double-ζ with polarization functions basis set (DZP) has been used.

Because of the DFT limitations, a further extension beyond the local density approximation (LDA) is carried out using the LDA+U method, which greatly improves the description of the localized states. The LDA+U method has been applied to similar systems[17,18] using the same calculation methodology.[17] We use periodic boundary conditions with 18 special k points in the irreducible Brillouin zone. For almost all calculations a zinc-blende ZnS experimental lattice constant of 5.41 Å has been assumed.

III. RESULTS

The study presented in this work is based on $S_{32}Zn_{30}Cr_2$ materials. The crystalline structure used by the host semiconductor is a 64-atom cubic cell $S_{32}Zn_{32}$. In this cell two Zn atoms have been substituted by two Cr atoms, located as far as possible from each other. In this structure the atomic environment of the transition-metal atoms has a tetrahedral symmetry considering their immediate neighbors. The S atoms can be broken down into two groups: those directly bonded to the Cr atoms (S_1) and those which are not (S_2).

Using the methodology described in the computational methods section we have carried out an extensive analysis of the electronic properties for both ferromagnetic and antiferromagnetic spin alignments. The ferromagnetic spin order energy per cell is only 0.09 eV smaller than the antiferromagnetic. These theoretical values compare well with 0.096 eV in the literature for Cr-doped ZnS.[8]

A. LDA results

1. Energy band diagrams

The energy band diagram in some directions of the Brillouin zone (BZ) is shown in Fig. 2. An isolated IB, made up of the majority-spin component, appears between one full band (VB) and the empty band (CB) for both the ferromagnetic and antiferromagnetic spin orders. The Fermi energy (horizontal line in the figure) cuts this IB, showing that the band is partially full. Therefore, a sufficiently high density of Cr into ZnS substituting Zn atoms leads to the formation of an IB that suppresses the nonradiative recombination. This fact has been demonstrated experimentally.[9]

Every S, Zn, and Cr atom contributes with 6, 12, and 6 valence electrons, respectively (the atomic configurations of S, Zn, and Cr are $3s^2 3p^4$, $3d^{10}4s^2$, and $3d^5 4s^1$, respectively). Therefore, the $S_{32}Zn_{30}Cr_2$ cell has 564 electrons. For the ferromagnetic alignment, the first 278 minority-spin valence bands are full. For the majority-spin bands, there are 282 valence bands full and a group made up of six bands (283–288) with four electrons (two holes). This group makes up the partially filled intermediate band. The integrated number of states between the Fermi energy and the top of the IB is exactly 2, corresponding to two holes in the IB. This group makes up the partially filled intermediate band. Therefore, the charge difference between the majority- and minority-spin bands is eight electrons. For antiferromagnetic alignment, the first 280 valence bands are full. There is a group made up of three bands (281–283) with two electrons (one hole) in the gap. This group makes up the partially filled intermediate band for the antiferromagnetic alignment.

The IB principally arise as a consequence of the interaction between the crystalline potential and spin interaction

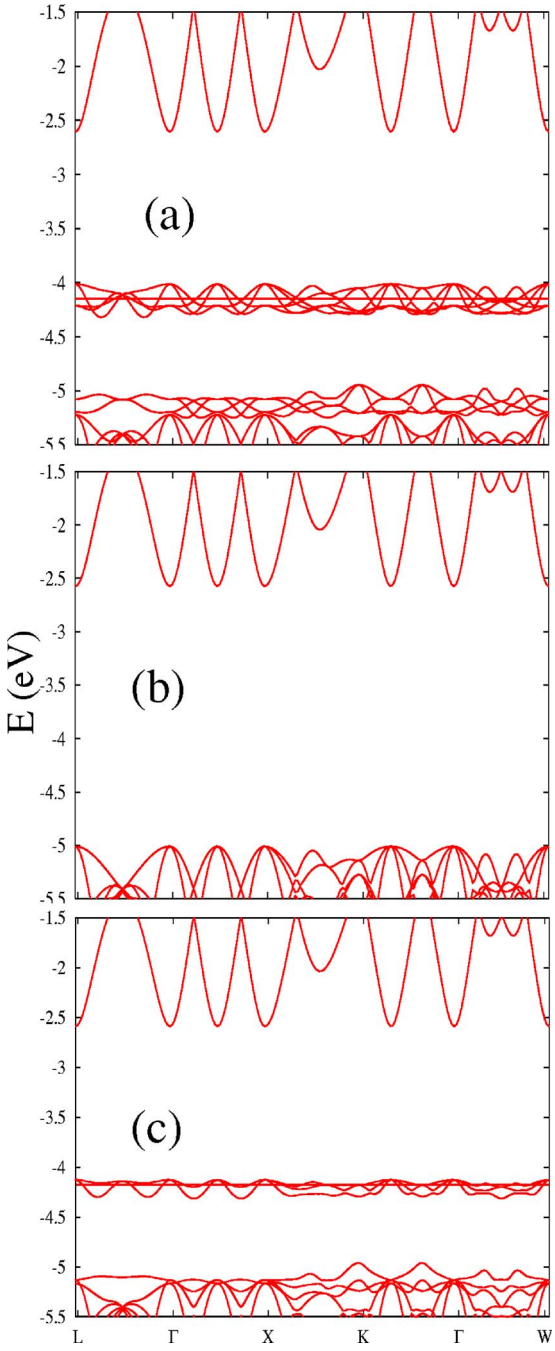

FIG. 2. (Color online) Energy bands (eV) in several directions of the Brillouin zone: (a) spin up, ferromagnetically aligned, (b) spin down, ferromagnetically aligned, and (c) antiferromagnetically aligned. The horizontal line in the (a) and (c) panels is the Fermi energy (E_F).

with transitions metal d orbitals. The transition-metal atom d orbitals are split into two groups (e and t) for each spin because of the approximately tetrahedral crystal potential around the transition-metal atom. The t group is made up of d_{xy}, d_{xz}, and d_{yz} orbitals and the e group of d_{z^2} and $d_{x^2-y^2}$ orbitals. Therefore, the three bands that make up the IB are a t group. The interaction of these metal orbitals with other orbitals of appropriate symmetry, in particular with the p S_1 orbitals with t symmetry, will produce bands whose width depends on the magnitude of the interaction. The more important difference between the ferromagnetic and antiferromagnetic alignments, besides spin order, is the band gaps and the width of the IB.

TABLE I. Energies (eV) for ferromagnetic (F) and antiferromagnetic (A) spin order. $\Delta E_{VI}^{(+)}$, $\Delta E_{IC}^{(+)}$, and $\Delta E_{I}^{(+)}$ are the VB-IB gap, the IB-CB gap, and the IB width for the majority-spin component. $\Delta E_{VC}^{(-)}$ is the VB-CB gap for the minority-spin component.

Spin order	$\Delta E_{VI}^{(+)}$	$\Delta E_{I}^{(+)}$	$\Delta E_{IC}^{(+)}$	$\Delta E_{VC}^{(+)}$	$\Delta E_{VC}^{(-)}$
F	0.62	0.31	1.41	2.34	2.43
A	0.64	0.18	1.54	2.36	

These properties are shown in Table I. For the majority-spin component (+) with an IB, $\Delta E_{VI}^{(+)}$, $\Delta E_{I}^{(+)}$, $\Delta E_{IC}^{(+)}$, and $\Delta E_{VC}^{(+)}$ are the gaps between the VB maximum and the IB minimum, the IB bandwidth (the difference between the IB maximum and minimum), the gap between the IB maximum and the CB minimum, and the gap between the VB maximum and the CB minimum ($\Delta E_{VC}^{(+)}=\Delta E_{VI}^{(+)}+\Delta E_{I}^{(+)}+\Delta E_{IC}^{(+)}$). Similarly, $\Delta E_{VC}^{(-)}$ is the gap between the VB maximum and the CB minimum for the minority-spin component.

The main difference between the two spin orders is that the IB bandwidth is smaller for the antiferromagnetic alignment. Therefore, the correlation effects will be larger for antiferromagnetic alignment. In fact, when correlations effects are introduced with a screened Coulomb interaction, the ferromagnetic spin order is more stable than the antiferromagnetic. The gap between the VB and CB is lower than the experimental gap of the host semiconductor. As is well known, the DFT underestimates the band gap and overestimates the bandwidth. This fact could strengthen the results obtained with respect to the presence of the intermediate bands in these compounds. For this reason the band gap values are lower than the experimental one. In this work, no correction for the band gap underestimation was made with scissor operators. Recent results in materials with an IB and with a higher metal-transition concentration[7] show that when LDA+U and LDA-SIC are used, the IB is maintained. This fact will also be demonstrated later with the LDA+U method.

2. DOS and population analysis

The main characteristic near the Fermi energy is the presence of an isolated IB. In order to identify the orbital composition of these bands the projected density of states (DOS) of the atoms and the t, e, and p Cr orbitals [Fig. 3(c)] is represented in Fig. 3. The contribution of the atoms to the IB in upward order is S_2, S_1, and Cr [Figs. 3(a) and 3(b)]: the IB is made up of Cr orbitals and the S_1 orbitals directly bonding to Cr atoms. This IB has t symmetry. Therefore, the IB is made up mainly of the combination of the t (d_{xy}, d_{xz}, and d_{yz}), a small contribution of p Cr orbitals and p S_1 orbitals, also of t symmetry. In Fig. 3(c) we can also see that the VB top has a great contribution of the e Cr orbitals: d_{z^2} and $d_{x^2-y^2}$. These general characteristics are common for both the ferromagnetic and antiferromagnetic spin orders.

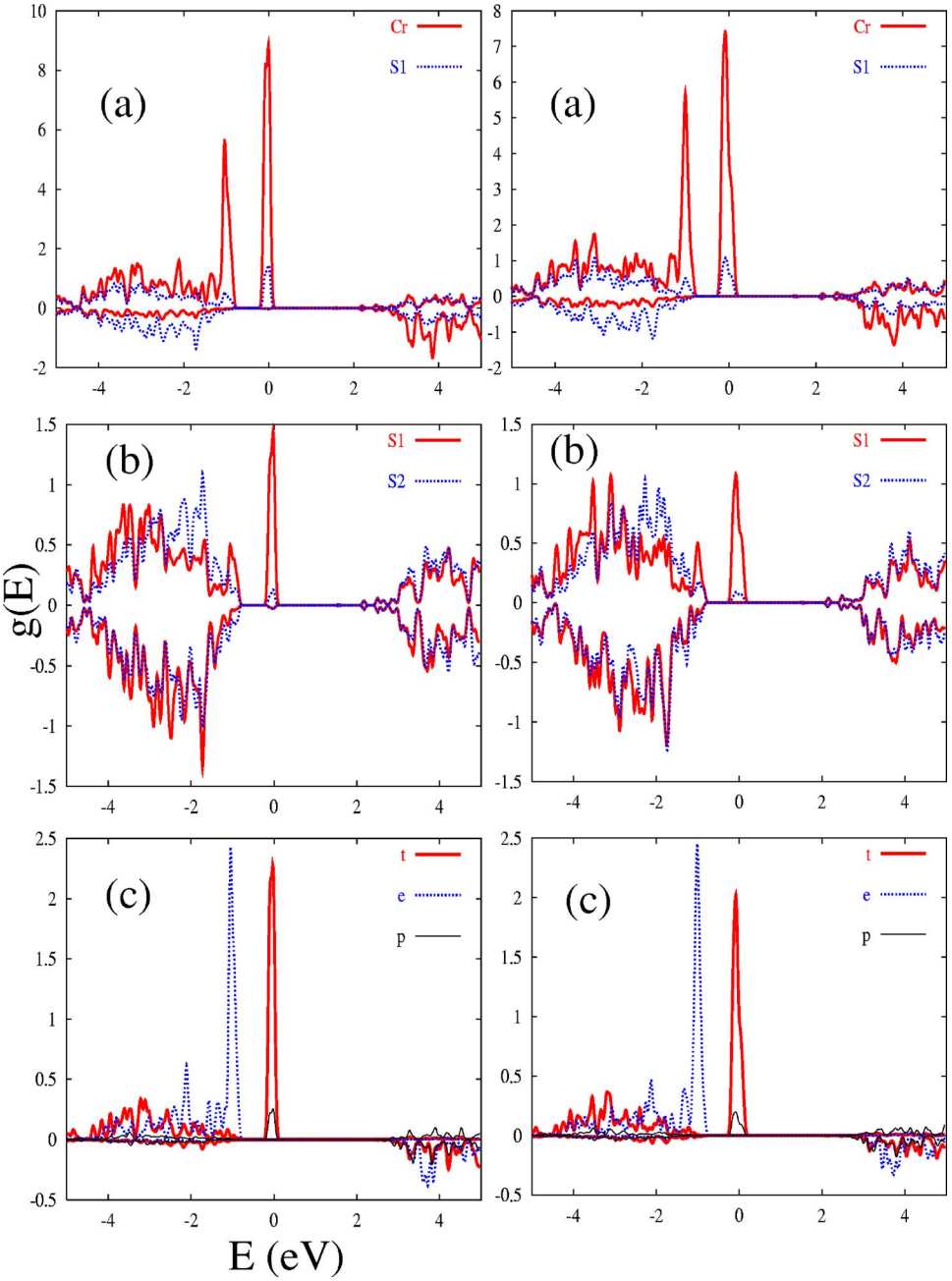

FIG. 3. (Color online) Projected DOS (a) on Cr and S_1 atoms, (b) on S_1 and S_2 atoms, and (c) on t, e, and p Cr orbitals. The left and right panels correspond to the antiferromagnetic and ferromagnetic spin orders, respectively. The Fermi energy as zero has been chosen in this figure. The DOS above and below the zero horizontal axis correspond to majority and minority spins, respectively.

In order to confirm the DOS results, a Mulliken population analysis of Cr, S, and Zn atoms is shown in Table II. First we can see that the atomic and orbital charges for S atoms are similar for ferromagnetic and antiferromagnetic spin alignments. The atomic charge associated with the S atoms directly bonded with the Cr atom (S_1 atoms) is smaller than the other S atoms (S_2). Moreover, the polarization of the S_2 atoms is almost zero, whereas the polarization of the S_1 atoms has a different sign than the Cr and Zn atoms for the ferromagnetic order. Except in the spin order of the Cr atoms and the t and e orbital charges, the charges for the other orbitals and alignments are very similar. For ferromagnetic order, it can be seen that the d Cr orbitals that have more charge associated are, in decreasing order, the e, t, and p orbitals. It indicates that the spin-up components of the Cr atom contribute below the Fermi energy to the VB and IB, whereas the spin-down components contribute to the CB. The Cr majority-spin component, with an IB, also has a greater charge than the minority-spin component.

3. Magnetization

The magnetization of the unit cell for the $S_{32}Zn_{30}Cr_2$ system is $8\mu_B$, and the magnetic moments per atom are $m_{Cr} \approx +4.26\mu_B$, $m_{S1} = -63.0 \times 10^{-3}\mu_B = -14.8 \times 10^{-3} m_{Cr}$, $m_{S2} = -6.0 \times 10^{-3}\mu_B \sim -1.4 \times 10^{-3} m_{Cr}$, and $m_{Zn} = 5.0 \times 10^{-3}\mu_B \sim 1.2 \times 10^{-3} m_{Cr}$ respectively. The Cr enters cation sites and two of its electrons are given to the bonds, thus forming the deep impurity level $Cr^{2+}(3d^4)$. Using the free-ion model, the ground configuration is $^5D_0$ according to Hund's rules. The crystalline field further splits this configuration into a multiplet of symmetry T_2 and a multiplet E. Therefore, the magnetic moment of the Cr atom in this alloy is lower than

TABLE II. Mulliken population analysis for Cr_1, Cr_2, S_1, and S_2 atoms (q) and s, t, e, and p orbitals with ferromagnetic (F) and antiferromagnetic (A) spin order for the $S_{32}Zn_{30}Cr_2$ system. The spin component is shown in brackets: + for majority and − for minority spin respectively.

Atom	F/A	$q(+)$	$s(+)$	$t(+)$	$e(+)$	$p(+)$	$q(-)$	$s(-)$	$t(-)$	$e(-)$	$p(-)$
Cr_1	F	5.18	0.36	0.80	0.96	0.16	0.92	0.32	0.08	0.02	0.11
Cr_2	F	5.18	0.36	0.80	0.96	0.16	0.92	0.32	0.08	0.02	0.11
S_1	F	3.07	0.83	0.02	0.02	0.71	3.13	0.84	0.01	0.01	0.74
S_2	F	3.13	0.84	0.02	0.01	0.73	3.14	0.84	0.02	0.01	0.74
Cr_1	A	5.17	0.37	0.78	0.96	0.16	0.93	0.33	0.07	0.02	0.11
Cr_2	A	0.93	0.33	0.07	0.02	0.11	5.17	0.37	0.78	0.96	0.16
S_1	A	3.07	0.83	0.02	0.02	0.71	3.13	0.84	0.01	0.01	0.74
S_2	A	3.13	0.84	0.02	0.01	0.73	3.13	0.84	0.02	0.01	0.74

expected from the free-ion picture because of the overlap and the polarization of the S atoms, negative with respect to that of Cr. In Fig. 4 we present the radial distribution of magnetization around the Cr and S atoms. The radial magnetization is calculated as

$$m(r) = \int_{\Omega} [\rho_+(\mathbf{r}) - \rho_-(\mathbf{r})] d\mathbf{r},$$

where Ω is a sphere of radius r and ρ_σ is the charge density for spin σ. Therefore, this radial distribution depends on the radius r from the atom considered and the difference between the majority and minority charge densities. For the Cr, the magnetization saturates around $r_S^{(Cr)}=2.0$ Å [the inset in Fig. 4(a)]. This value is approximately $m_{Cr}\approx 4.26\mu_B$. Note that we cannot say anything about the saturation radius of the S_1, S_2, and Zn atoms because their magnetization values are similar and smaller than the Cr atom magnetization.

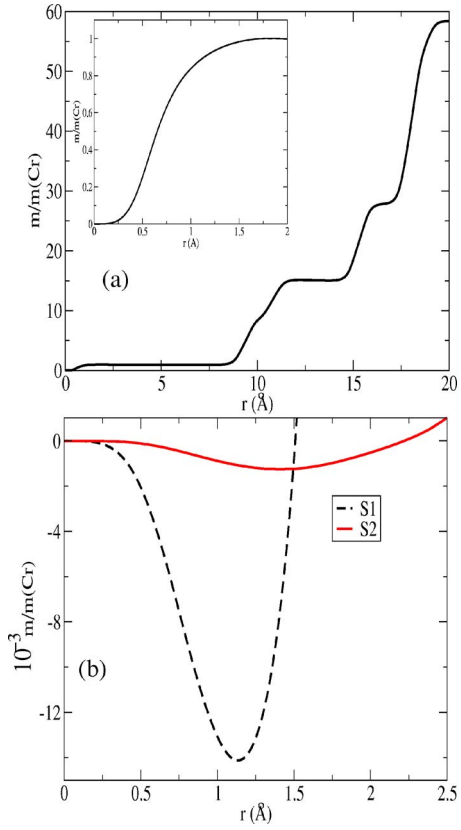

FIG. 4. (Color online) Radial distribution of magnetization within a sphere of radius r placed at (a) Cr and (b) S_1 and S_2 atoms. The inset in panel (a) shows the Cr distribution with a smaller range. The units of the radial distribution are scaled respect to the saturation value of the Cr atom.

The increase in the radial distribution depends on the number of atoms surrounding to the atom taken as origin and the magnetization of these atoms. However, as the Cr magnetization is larger than the S and Zn atoms, the number of Cr atoms included in the radial distribution will mainly determine the value of this radial distribution. For example, the Cr atom is surrounded by 4 S_1, 12 Zn, 12 S_2, 6 Zn, and 12 S_2 atoms for distances around 2.34, 3.82, 4.48, 5.41, and 5.89 Å. The value of the radial distribution is determined within this range by the Cr atom [Fig. 4(a)]. However, for 9.37, 10.82, 15.30, 17.94, and 18.74 Å it increases greatly because of the following Cr shells with 8, 6, 12, 24, and 8 atoms, respectively. Therefore, for these distances the magnetization is approximately 9, 15 (=9+6), 27 (=15+12), 51, and 59.

In contrast, the radial magnetization of the S_1 atoms (bonded with Cr) has a negative minimum around 1.3 Å, followed by a sharp increase. For a distance of 2.34 Å the S_1 atom is surrounded by Cr+3Zn. The minimum corresponds to a negative polarization with respect to the Cr atom with an approximate value of $m_{S1}\sim -14.8\times 10^{-3} m_{Cr}$. From this minimum, the radial distribution increases because the polarization of the Cr atom starts to be included in the integration. For 3.3 Å (1.2 Å$+r_S^{(Cr)}$) approximately all the Cr polarization is included in the integral and the value of the radial polarization of the S_1 atom is approximately m_{Cr}.

The S_2 atom also shows a similar behavior [Fig. 4(b)] with a negative minimum around 1.4 Å corresponding approximately to $-1.4\times 10^{-3} m_{Cr}$, the magnetization m_{S2} of the S_2 atom. The S_2 atom is surrounded by several shells: 4 Zn at 2.34 Å, 3 S_1+9 S_2 at 3.82 Å, Cr+11 Zn at 4.48 Å, 2 S_1+4 S_2 at 5.41 Å, Cr+11 Zn at 5.89 Å, etc. Therefore, the first negative minimum at 1.4 Å corresponds to the S_2 magnetization with a value approximately m_{S2}. Later, the radial magnetization increases with r because of the positive polarization of the 4 Zn atoms in the first shell, then decreases slightly because of the negative polarization of the S

TABLE III. Energies (eV) for $U=0$, 3, 6, and 9 eV. $\Delta E_{VI}^{(+)}$, $\Delta E_{IC}^{(+)}$, and $\Delta E_{I}^{(+)}$ are the VB-IB gap, the IB-CB gap, and the IB width for the majority-spin component. $\Delta E_{VC}^{(-)}$ is the VB-CB gap for the minority-spin component.

U	$\Delta E_{VI}^{(+)}$	$\Delta E_{IC}^{(+)}$	$\Delta E_{I}^{(+)}$	$\Delta E_{VC}^{(+)}$	$\Delta E_{VC}^{(-)}$
0	0.65	1.41	0.30	2.36	2.43
3	0.54	1.34	0.50	2.38	2.41
6	0.45	1.29	0.69	2.43	2.38
9	0.40	1.18	0.83	2.41	2.37

atoms in the second shell and increases abruptly when the Cr atom in the third shell is included in the integral of the radial distribution. The value of the radial polarization of the S_2 atom at this distance $(5.89+r_S^{(\mathrm{Cr})})$ is approximately m_{Cr}.

In order to analyze whether a Jahn-Teller distortion splits the occupied and empty IB states, the cell-internal atom positions were allowed to relax according to the calculated quantum mechanical forces (without any symmetry constraints) until the total energy minimum was reached and the forces became smaller than 0.004 eV/Å. The relaxing of the atomic configurations causes a slight increase in IB width and a slight decrease in the gaps. Hence, a distortion driven by atomic relaxing that splits the occupied and empty IB states is not observed.

B. LDA+U results

At the level of dilution studied in this work and because of the partially full IB, correlation effects are very important. Because of the DFT limitations, further extension beyond the LDA will be necessary to estimate the corrections to bandwidths and excitation spectra. The analysis of the correlation effects is a difficult theoretical problem. The main limitation of other, more sophisticated, methods[7] is the very high computational cost, making this type of calculation almost prohibitive except for the simplest material systems. At an intermediate level, the LDA combination with a Hubbard term greatly improves the description of the localized states. The method with a screened Coulomb interaction (U) has been applied for it. The main consequence when applying the LDA+U method is that the antiferromagnetic alignment is less stable than the ferromagnetic (around 0.09–0.19 eV per cell with U between 0 and 9 eV) and the t IB merges with the VB. Therefore we will focus our study on the ferromagnetic alignment from here on.

The gaps and bandwidths for $U=0$, 3, 6, and 9 eV and the two spin components for the ferromagnetic order are shown in Table III. As U increases from 0 to 9 eV, a decrease of $\Delta E_{VI}^{(+)}$ and $\Delta E_{IC}^{(+)}$ and an increase in the bandwidth $\Delta E_{I}^{(+)}$ can be seen. The $\Delta E_{VC}^{(+)}$ and $\Delta E_{VC}^{(-)}$ gaps are lower than the experimental host semiconductor gap. It is necessary to point out that the LDA+U method does not correct the spurious self-interaction. Therefore, when this self-interaction is corrected, the width of the IB will diminish and the gaps will increase. In this work, no correction for the band gap underestimation was made. Because of the decrease in $\Delta E_{IC}^{(+)}$, and as the number of electrons in the IB is constant, the Fermi energy decreases as U increases.

1. DOS and population analysis

Another effect of the LDA+U corrections is the modification of the relative composition of the d and p transition-metal orbitals making up the IB. The contribution of all the orbitals within each group to the IB is equal for $U=0$ eV (Fig. 3). However, the situation is different for $U\neq 0$ eV. In order to analyze these modifications, the projected DOS for t, e, and p orbital groups for $U=3$, 6 and 9 eV are shown in Fig. 5. In all cases the IB is made up mainly of t Cr metal-transition orbitals and with a lower proportion of p metal-transition orbitals. In all cases, the VB maximum also has an e transition-metal orbital character. It can be seen in Fig. 5 that the entire orbital contribution has more structure with an increase of U: the p, t, and e orbitals are split into several contributions. Therefore, in general, the degeneration is broken and the contribution to projected DOS will be different. The contribution of the d_{xz} orbital is split significantly with respect to the other t orbitals (d_{xy} and d_{yz}), with a more similar behavior. Note that for $U>6$ eV a splitting of the d_{xz} component produces two Hubbard subbands, a full one below the Fermi energy and an empty one above the Fermi energy. The lower band has a smaller contribution than the upper band. Therefore, the charge associated with the d_{xz} orbital will diminish with an increase in U. This fact will be confirmed below using the population analyses. However, the behavior with U is different for d_{xy} and d_{yz}. In these cases, although the orbital contribution has more structure with the increase in U, the splitting into two subbands does not happen. The two components have similar contributions above Fermi energy. Therefore, the charge of the d_{xy} and d_{yz} will not vary significantly with the increase in U and it will be similar for both.

For $U=0$ eV the contribution of the two e orbitals (d_{z^2} and $d_{x^2-y^2}$) is equal. An increase in U produces a different contribution to the projected DOS. With the increase in U, the edge of the VB increases the $d_{x^2-y^2}$ character slightly as well as decreasing the d_{z^2} character slightly. For these orbitals the charge is not modified substantially because their larger contribution is to the VB.

The variation in the contribution to the projected DOS of the p metal-transition orbitals with U is similar to the t metal-transition orbitals. An increase in U splits the contribution to the IB. Moreover, the contribution of the p_y orbital is split into two Hubbard subbands, similar to the d_{xz} orbital. Nevertheless, the effect on the p orbital charge is smaller than on the d orbitals because the contribution of the p orbitals to the IB is smaller than the contribution of the d orbitals.

For all U values, the total integrated DOS between the Fermi energy and the top IB is also two electrons, confirming the introduction of two holes into the IB. From the results, LDA+U modifies the relative composition of the d and p Cr orbitals, reducing the contribution at the Fermi energy and shifting the occupied and unoccupied bands to lower and higher energies, respectively.

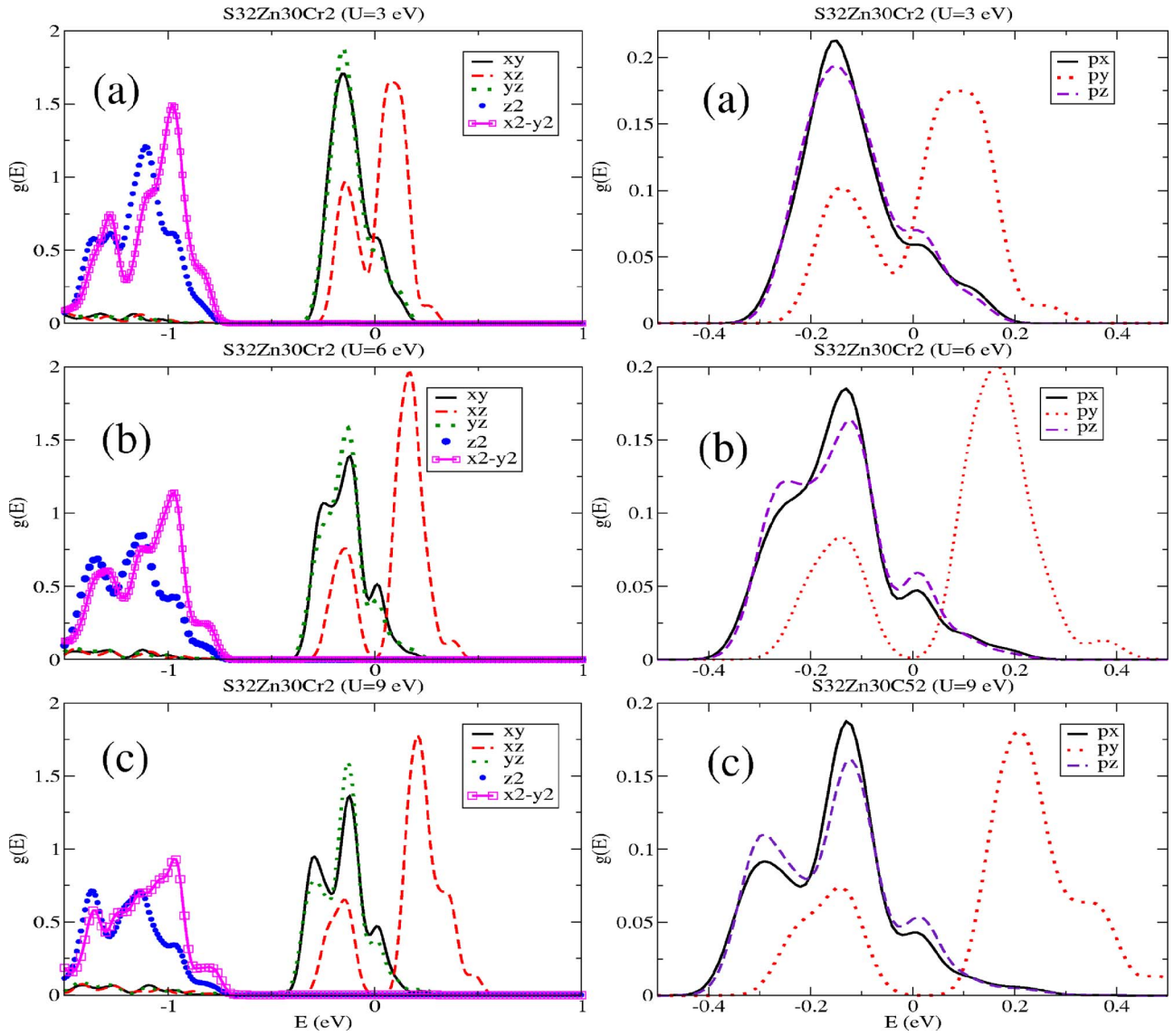

FIG. 5. (Color online) Projected DOS on d (left panels) and p (right panels) orbitals with (a) $U=3$ eV, (b) $U=6$ eV, and (c) $U=9$ eV. The Fermi energy as zero has been chosen in this figure.

In order to confirm the previous DOS results, Mulliken total and orbital population analysis is used to compare different U values (Table IV). Table IV shows this population analysis for $U=3$, 6, and 9 eV with respect to $U=0$ eV (Table II) and the two spin components (+ for majority and − for minority). Note that the charge variation for different U values and the variation between the orbitals of the same group (t, e, and p) are very small, of the order of 10^{-2} times the electron charge. From the table we see that the spin down (−) minority Cr charge increases with U. It produces an increase in the Cr polarization with U. The d_{xy} and d_{yz} charges practically do not vary and are almost equal. Similar behavior is seen with the two e Cr orbitals. However, the d_{xz} charge decreases with U for the two spin components with respect to $U=0$ eV. The p_x and p_z charges are also almost equal, whereas the p_y charge is slightly different because of the splitting into two Hubbard subbands where the upper subband above the Fermi energy does not contribute to the orbital charge. These analyses confirm the previous DOS results (Fig. 5).

2. Magnetization

The magnetization of the S_1 and S_2 atoms with and without screened Coulomb interactions is compared in Fig. 6. For all U values the unit cell magnetization is $8\mu_B$. However, the magnetization of the Cr atoms increases from $4.26\mu_B$ ($=m_{\mathrm{Cr}}$) for $U=0$ eV to $4.36\mu_B$ for $U=9$, and for the S_1 atoms it decreases from $-14.08\times10^{-3}m_{\mathrm{Cr}}$ for $U=0$ eV to $-18.7\times10^{-3}m_{\mathrm{Cr}}$ for $U=9$ eV. For S_2 atoms the variation is very small compared with the S_1 atoms. An increase in the minimum depth of the S_1 and S_2 atoms is seen. This increase is due to the polarization of the atoms, although of small value, decreasing with respect to the Cr atom. This effect is larger for S_1 (the magnetizations for S_1 and S_2 are in different scales in the figure).

TABLE IV. Difference between the Mulliken population analysis of Cr atoms (Q) and of Cr orbitals for $U=3$, 6, and 9 eV with respect to the population for $U=0$ eV. The spin component is shown in the second column: + for majority and − for minority-spin, respectively. The charge units are 10^2 times the electron charge.

U	spin	Q	s	d_{xy}	d_{xz}	d_{yz}	d_{z^2}	$d_{x^2-y^2}$	p_x	p_y	p_z
3	+	1	1	8	−18	8	0	0	1	−1	1
3	−	−5	1	−3	−3	−3	0	0	1	1	1
6	+	1	1	10	−24	10	1	1	2	−1	2
6	−	−8	2	−4	−4	−4	−1	−1	1	1	1
9	+	0	2	11	−26	1	1	1	2	−3	2
9	−	−10	2	−6	−5	−6	−1	−1	2	2	2

3. Electronic density

To conclude with the results, the difference between the electronic density distribution ($\Delta\rho=\rho_3-\rho_0$) corresponding to $U=3$ eV (ρ_3) and $U=0$ eV (ρ_0) is shown in Fig. 7 for the (110) lattice plane. This difference can be positive or negative. In the figure, $\Delta\rho$ has been broken down into contributions: (a) $\Delta\rho>0$ and (b) $-\Delta\rho>0$. The zone where there are level curves when $-\Delta\rho>0$ represents a decrease in the charge density for $U=3$ eV with respect to $U=0$ eV, and $\Delta\rho>0$ represents an increase. In Fig. 7(b), we can see a decrease in the electronic density at the Cr atom in the plane that contains the z axis and an increase in the xy plane and on the z axis [Fig. 7(a)]. These results are in accordance with previous DOS and population analyses. In conclusion, a flow of charge from the d_{xz} to the d_{xy} and d_{yz} orbitals happens as U increases. Note that the effect on the p orbitals is masked by the d orbitals, since the p orbitals have a smaller charge. This analysis confirms the previous projected DOS and population analysis results.

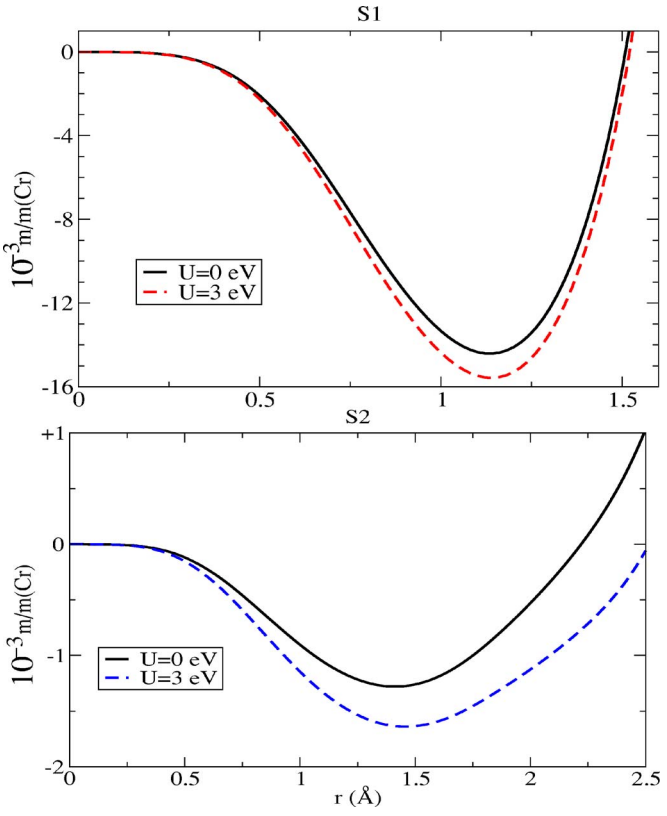

FIG. 6. (Color online) Radial distribution of magnetization within a sphere of radius r placed at S_1 and S_2 atoms with $U=0$ and 3 eV. The units of the radial distribution are scaled with respect to the saturation value of the Cr atom when $U=0$ eV.

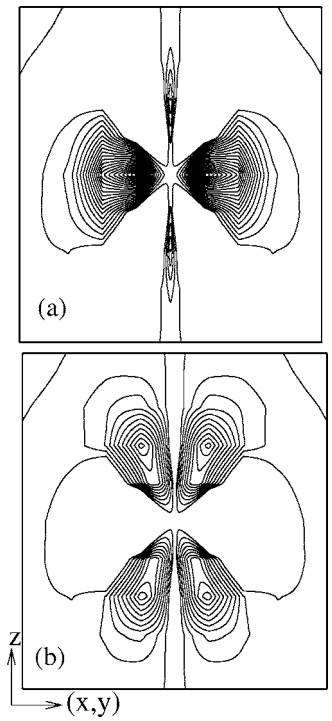

FIG. 7. Difference between the electronic density (electrons/Å^3) for $U=3$ eV and $U=0$ eV ($\Delta\rho=\rho_3-\rho_0$) for (a) $\Delta\rho>0$ and (b) $-\Delta\rho>0$, displayed for the (110) plane. The lowest contour corresponds to 2.21×10^{-2} electrons/Å^3 for (a) and 1.05×10^{-2} electrons/Å^3 for (b), and each contour is 10^{-3} times larger.

IV. CONCLUSIONS

The objective of this work has been to analyze and to relate the microscopic electronic properties with the characteristics of the high-efficiency solar cells and midinfrared lasers with low nonradiative decay, in particular those related to the partially full intermediate band present in a ZnS host semiconductor uniformly doped with Cr. From the results, it was found that these materials have a partially filled IB for both the ferromagnetic and antiferromagnetic spin alignments. The electronic density, the atomic and orbital composition of the band structure, the atomic and orbital population, and the magnetization have been analyzed, showing that this IB is mainly made up of a t-group orbital of the Cr transition-metal atom. These results are obtained using

different schemes to deal with the correlation problem. The addition of these corrections shows a larger stability of the ferromagnetic spin order and an increase in the bandwidth of the IB. However, an increase in the screened Coulomb interaction from 0 to 9 eV does not lead to a metal-insulator transition. Nevertheless, the splitting into two subbands happens for d_{xz} and p_y components. From these results, the IB of this material is longer insensitive to the increase in the self-repulsion compared with other II-VI semiconductors doped with Cr.[17]

ACKNOWLEDGMENTS

The author thankfully acknowledges the computer resources, technical expertise, and assistance provided by the Barcelona Supercomputing Center. This work has been supported by the European Commission through the funding of the project FULLSPECTRUM (Ref. No. SES6-CT-2003-502620) and by La Comunidad de Madrid through the funding of the project NUMANCIA (Ref. No. S-0505/ENE/0310).

*Electronic address: ctablero@etsit.upm.es

[1] A. Luque and A. Martí, Phys. Rev. Lett. **78**, 5014 (1997); A. Luque and A. Martí, Prog. Photovoltaics **9**, 73 (2001).
[2] W. Shockley and H. J. Queisser, J. Appl. Phys. **32**, 510 (1961).
[3] A. Martí, L. Cuadra, and A. Luque, in *Proceedings of the 28th IEEE Photovoltaics Specialists Conference* (IEEE, New York, 2000), p. 940.
[4] K. M. Yu, W. Walukiewicz, J. Wu, W. Shan, J. W. Beeman, M. A. Scarpulla, O. D. Dubon, and P. Becla, Phys. Rev. Lett. **91**, 246403 (2003).
[5] C. Tablero, Phys. Rev. B **72**, 035213 (2005); Sol. Energy Mater. Sol. Cells **90**, 203 (2006); **90**, 588 (2006); Comput. Mater. Sci. **36**, 263 (2006); Solid State Commun. **133**, 97 (2005).
[6] E. Kulatov, H. Nakayama, H. Mariette, H. Ohta, and Y. A. Uspenskii, Phys. Rev. B **66**, 045203 (2002); Y. A. Uspenskii, E. Kulatov, H. Mariette, H. Nakayama, and H. Ohta, J. Magn. Magn. Mater. **258-259**, 248 (2003).
[7] P. Mahadevan and A. Zunger, Phys. Rev. B **69**, 115211 (2004); C. Persson and A. Zunger, *ibid.* **68**, 073205 (2003).
[8] H. Katayama-Yoshida and K. Sato, J. Phys. Chem. Solids **64**, 1447 (2003); K. Sato, P. H. Dederichs, H. Katayama-Yoshida, and J. Kudrnovsky, Physica B **340-342**, 863 (2003).
[9] L. D. DeLoach, R. H. Page, G. D. Wilke, S. A. Payne, and W. F. Krupke, IEEE J. Quantum Electron. **32**, 885 (1996).
[10] A. Luque, A. Martí, E. Antolín, and C. Tablero, Physica B **382**, 320 (2006).
[11] W. Kohn and L. J. Sham, Phys. Rev. **140**, A1133 (1965).
[12] J. M. Soler, E. Artacho, J. D. Gale, A. García, J. Junquera, P. Ordejon, and D. Sánchez-Portal, J. Phys.: Condens. Matter **14**, 2745 (2002); E. Artacho, D. Sánchez-Portal, P. Ordejón, A. García, and J. M. Soler, Phys. Status Solidi B **215**, 809 (1999); D. Sánchez-Portal, E. Artacho, and J. M. Soler, Int. J. Quantum Chem. **65**, 453 (1997); P. Ordejón, E. Artacho, and J. M. Soler, Phys. Rev. B **53**, R10441 (1996).
[13] D. M Ceperley and B. J. Alder, Phys. Rev. Lett. **45**, 566 (1980).
[14] N. Troullier and J. L. Martins, Phys. Rev. B **43**, 1993 (1991).
[15] L. Kleinman and D. M. Bylander, Phys. Rev. Lett. **48**, 1425 (1982); D. M. Bylander and L. Kleinman, Phys. Rev. B **41**, 907 (1990).
[16] O. F. Sankey and D. J. Niklewski, Phys. Rev. B **40**, 3979 (1989).
[17] C. Tablero, J. Chem. Phys. **123**, 114709 (2005); **123**, 184703 (2005).
[18] M. Wierzbowska, D. Sánchez-Portal, and S. Sanvito, Phys. Rev. B **70**, 235209 (2004); A. Filippetti, N. A. Spaldin, and S. Sanvito, Chem. Phys. **309**, 59 (2005); L. M. Sandratskii, P. Bruno, and K. Kudrnovsky, Phys. Rev. B **69**, 195203 (2004).